

Calibration of Energy Density Functionals with Deformed Nuclei

N. Schunck,¹ J. O’Neal,² M. Grosskopf,³ E. Lawrence,³
S.M. Wild²

¹ Nuclear and Chemical Science Division, Lawrence Livermore National Laboratory,
Livermore, CA 94551, USA

² Mathematics and Computer Science Division, Argonne National Laboratory,
Lemont, IL 60439, USA

³ Computer, Computational, and Statistical Sciences Division, Los Alamos National
Laboratory, Los Alamos, NM 87545, USA

E-mail: schunck1@llnl.gov

Abstract. Nuclear density functional theory is the prevalent theoretical framework for accurately describing nuclear properties at the scale of the entire chart of nuclides. Given an energy functional and a many-body scheme (e.g., single- or multireference level), the predictive power of the theory depends strongly on how the parameters of the energy functionals have been calibrated with experimental data. Expanded algorithms and computing power have enabled recent optimization protocols to include data in deformed nuclei in order to optimize the coupling constants of the energy functional. The primary motivation of this work is to test the robustness of such protocols with respect to some of the technical and numerical details of the underlying calculations, especially when the calibration explores a large parameter space. To this end, we quantify the effect of these uncertainties on both the optimization and statistical emulation of composite objective functions. We also emphasize that Bayesian calibration can provide better estimates of the theoretical errors used to define objective functions.

Keywords: Density functional theory, Self-consistent calculations, Bayesian calibration, Optimized energy density functionals, Skyrme functionals, Supervised learning

Submitted to: *J. Phys. G: Nucl. Phys.*

1. Introduction

Nuclear theory plays an essential role in many fundamental science problems [1]. In particular, it provides data for simulations of the origin of the elements in astrophysical environments, particularly the rapid-neutron capture process, which involves very neutron-rich, short-lived nuclei for which no experimental measurements exist [2].

Current research on a possible end for the periodic table of elements also involves advanced nuclear calculations for superheavy elements, where fission plays a major role [3]. Tests of fundamental symmetries and the search for physics beyond the Standard Model also often depend on high-accuracy, high-precision calculations of nuclear properties [4, 5].

A common feature of all theoretical nuclear models is that they are imperfect. In this work, we focus on nuclear energy density functional theory (DFT), which relies on an effective description of nuclear forces encapsulated in the form of an energy density functional (EDF) and is the prevalent framework for computing heavy nuclei [6]. Because of the disconnect between realistic nuclear potentials and the effective encoding of many-body effects in the functional, DFT should be viewed as a phenomenological model with unknown parameters that must be calibrated with a set of experimental data (see, e.g., [7, 8, 9, 10, 11, 12, 13, 14]). This naturally induces uncertainties and errors that have been extensively discussed in the literature [15, 16, 17, 18].

Traditionally, energy functionals were often fitted to nuclear matter properties together with a small sample of properties in doubly magic, closed-shell nuclei (see, e.g., [19, 20, 21, 22]). In addition to the advantage in computational cost, this strategy was often justified by the fact that (i) in such nuclei, pairing correlations (e.g., as described by Bardeen–Cooper–Schrieffer (BCS) or the Hartree-Fock-Bogoliubov (HFB) theory) automatically collapse: the parameters of the pairing functional (particle-particle channel) are thus decoupled from the ones of the mean field (particle-hole channel), and (ii) the shell effects that determine many deformation properties of nuclei originate from the spontaneous symmetry breaking of rotational invariance: if the spherical shell structure is properly reproduced, deformed shell gaps will automatically appear for the correct number of particles. The success of “single-particle phenomenology” in describing broad swaths of nuclear properties gave credence to this approach; see, for example, [23] for an overview.

As traditional computational bottlenecks in DFT applications slowly disappear, this naïve approach to EDF calibration has been questioned [9]. In particular, the importance of the spherical shell structure can be nuanced for at least three reasons. First, single-particle levels are not experimental observables [24]: not only are they extracted from experimental data in a model-dependent way, but for all except the Hartree-Fock (HF) theory they cannot be unambiguously related to actual observables of the model [6, 25]. Second, several studies have shown that correlations beyond HF (e.g., particle-vibration couplings) have a large impact on such shell structure [26, 27, 28]: forcing a fit at the HF level will thus cause overfitting. Misfits are unavoidable, and it is thus highly unlikely that one could reproduce exactly a given shell structure (a problem recognized also in nuclear phenomenology; see [29, 30, 31]). Third, deformation properties are the result of a competition between shell and bulk (liquid-drop) effects: the analyses of [32, 33] show that bulk surface properties, particularly isovector ones, can be constrained only by calculations in very deformed nuclei. Performing a fit in deformed nuclei thus seems unavoidable, since it reflects the fact the HFB theory is an imperfect model that must

be carefully calibrated with all types of observables that fall within its scope.

In the important case where fitting involves deformed HF or HFB calculations, careful examination is warranted to determine how the self-consistent iterative process is initialized. In other applications, such as fission, these initial conditions are known to be crucial [34]: for a given parameterization of the functional, does every HFB calculation in the fit converge to an appropriate value? In other words, are all deformed nuclei really deformed? Are fission isomers truly separated from the ground state by a barrier? Such questions can be especially relevant for methods based on supervised learning, where the training of the model involves exploring a large section of the parameter space, some regions of which may lead to nonphysical results.

The goal of this paper is thus to study the robustness of the optimization and calibration protocols that include deformed nuclei. Specifically, we focus on the calibration of the Skyrme UNEDF1 functional. We seek to (i) quantify the impact of changes in initial conditions for the underlying HFB calculations on this function (i.e., the “forward model”); (ii) analyze the behavior of an optimization algorithm for the inverse problem under such changes; and (iii) quantify the impact on the training of statistical models in the context of Bayesian calibration.

In Section 2 we review some basic elements of nuclear density functional theory, the UNEDF1 functional, and the optimization software based on the HFBTHO solver. In Section 3 we detail the case study considered here, which varies the deformation of the initial state in HFB calculations while keeping conditions such as the dataset, platform, and parameter set constant. In Section 3 we also study the effect of these changes on the forward computation and optimization-based solution of the inverse problem. In Section 4 we study both the effect on statistical emulation with Gaussian processes (GPs) and the downstream effect on GP-based calibration.

2. Theoretical and Computational Background

The general physics framework for this and all previous UNEDF work is the HFB theory, where the nuclear many-body wave function has the form of a quasiparticle vacuum; see [6] for a review.

2.1. The Hartree-Fock-Bogoliubov Theory with Skyrme Generators

In the HFB theory, the one-body density matrix and pairing tensor are the main degrees of freedom. The total energy of the nucleus at the HFB approximation can thus be expanded as

$$E[\rho, \kappa, \kappa^*] = E_{\text{nuc}}[\rho] + E_{\text{Cou}}[\rho] + E_{\text{pair}}[\kappa, \kappa^*]. \quad (1)$$

For the nuclear part of the energy functional (1), we consider a Skyrme-like EDF,

$$E_{\text{nuc}}[\rho] = \sum_{t=0,1} \int d^3\mathbf{r} \chi_t(\mathbf{r}),$$

where the functional includes the kinetic energy term and is expressed as

$$\chi_t(\mathbf{r}) = C_t^{\rho\rho} \rho_t^2 + C_t^{\rho\tau} \rho_t \tau_t + C_t^{JJ} J_t^2 + C_t^{\rho\Delta\rho} \rho_t \Delta\rho_t + C_t^{\rho\nabla J} \rho_t \nabla \cdot \mathbf{J}_t.$$

Here, the index t refers to the isoscalar ($t = 0$) or isovector ($t = 1$) channel. The definitions of the various densities ρ , τ , and \mathbf{J} (\mathbf{J} is the vector part of \mathbf{J}) can be found in [35, 36, 37, 38, 39]. The parameters of the model are the coupling constants $C_t^{uu'}$, all of which are real-valued scalars with the exception of $C_t^{\rho\rho}$, which has a density dependency of the form

$$C_t^{\rho\rho} = C_{t0}^{\rho\rho} + C_{tD}^{\rho\rho} \rho_0^\gamma(\mathbf{r}).$$

The full description of the particle-hole channel requires 13 parameters.

The Coulomb term in (1) is computed at the HF approximation with the exchange term treated with the Slater approximation [37]. The pairing energy is computed at the HFB approximation with an approximate Lipkin-Nogami correction based on a simple seniority pairing force; see [40, 41] for details. The pairing functional itself originates from a surface-volume density-dependent pairing force

$$V_q(\mathbf{r}, \mathbf{r}') = V_0^q \left[1 - \frac{1}{2} \frac{\rho(\mathbf{r})}{\rho_c} \right] \delta(\mathbf{r} - \mathbf{r}'),$$

where q indicates the type of particle (proton or neutron) and $\rho_c = 0.16 \text{ fm}^{-3}$. Including the pairing channel in the fit thus adds two more parameters, resulting in a total of 15 parameters.

2.2. The UNEDF1 Energy Functional

In the UNEDF optimization protocol described in [9, 10, 13], the coupling constants $C_{t0}^{\rho\rho}$, $C_{tD}^{\rho\rho}$, γ , and $C_t^{\rho\tau}$ are expressed as a function of the parameters of infinite nuclear matter [9]. As a result, the vector \mathbf{x} of parameters that can be adjusted in UNEDF fits is

$$\left(E^{\text{NM}}, \rho_{\text{sat}}, K^{\text{NM}}, a_{\text{sym}}^{\text{NM}}, L_{\text{sym}}^{\text{NM}}, 1/m_s^*, 1/m_v^*, C_0^{\rho\Delta\rho}, C_1^{\rho\Delta\rho}, C_0^{\rho\nabla J}, C_1^{\rho\nabla J}, C_0^{JJ}, C_1^{JJ}, V_0^n, V_0^p \right).$$

In all UNEDF fits, the vector effective mass was kept constant at the SLy4 value of $m_v^* = 1.249838$; see [21] for details. In the UNEDF0 and UNEDF1 fits, the tensor coupling constants were set to 0 (i.e., $C_0^{JJ} = C_1^{JJ} = 0$), reducing the number of fit parameters to 12.

The χ^2 criterion that defines an optimization's objective function and enters the expression for the likelihood is

$$\chi^2(\mathbf{x}) = \frac{1}{n_d - n_x} \sum_{i=1}^{D_T} \sum_{j=1}^{n_i} \left(\frac{s_{ij}(\mathbf{x}) - d_{ij}}{\sigma_i} \right)^2, \quad (2)$$

where n_x is the number of fit parameters, D_T is the number of data types, n_i is the number of data points for the data type i , n_d is the total number of data points (i.e., $n_d = \sum_{i=1}^{D_T} n_i$), $s_{ij}(\mathbf{x})$ is the simulation output for the point j of data type i , d_{ij} is the corresponding experimental value, and σ_i the estimate of the error for data type i . We recall that UNEDF1, the paradigm studied below, had the following characteristics.

- $n_x = 12$ for the original UNEDF1 fit in [10];
- $D_T = 4$ with binding energies ($i = 1$), proton r.m.s. radii ($i = 2$), odd-even staggering (OES) energy ($i = 3$), and excitation energy of fission isomers ($i = 4$);
- $n_d = 115$ —see supplemental material of [13] for details of the nuclei included;
- $\sigma_1 = 2$ MeV, $\sigma_2 = 0.02$ fm, $\sigma_3 = 0.05$ MeV, and $\sigma_4 = 0.5$ MeV, for masses, proton radii, OES, and fission isomers, respectively.

In contrast to the original UNEDF1 paper [10], we also use the AME 2016 mass evaluation [42] for all binding energies. To extract nuclear binding energies from results tabulated in the mass evaluation, we subtract the electronic binding energy for which we use the empirical formula

$$B_e(Z) = 1.44381 \times 10^{-5} Z^{2.39} + 1.55468 \times 10^{-12} Z^{5.35},$$

with the energy given in MeV. We include only true experimental measurements and do not take into account evaluated masses.

2.3. The HFBTHO Solver

Our DFT solver was based on the latest version of the HFBTHO program [43]. HFBTHO solves the HFB equation by expanding the solutions in the harmonic oscillator basis and by using successive diagonalizations of the HFB matrix until convergence (within a numerical tolerance) is achieved. Throughout this manuscript, we will refer to a *nuclear configuration* as a HFB solution for a nucleus with Z protons and N neutrons corresponding to a local minimum of the potential energy curve as a function of the axial quadrupole moment. For a single nuclear configuration and a given point \mathbf{x} in the functional's n_x -dimensional parameter space, HFBTHO calculates theoretical observable values $s_{ij}(\mathbf{x})$ for the binding energy, proton r.m.s. radius, proton pairing gap, and neutron pairing gap entering the objective function (2). For a given parameterization \mathbf{x} , the resulting value of the objective function is contingent on both the precision and the accuracy of the underlying HFB calculation.

- The *numerical precision* depends on a number of “hyperparameters” characterizing the basis (e.g., oscillator length b_0 , basis deformation β_{HO} , number of shells N_0 , number of states N_{states}), and quadrature grid (number of points for Hermite, Laguerre, and Legendre quadratures). In this work, we adopt the same conventions as in [9, 10, 13] concerning the basis characteristics. Specifically, we set $b_0 = \sqrt{\hbar/m\omega_0}$ using $\omega_0 = 1.2 \times 41/A^{1/3}$ (see, e.g., [44]), $N_0 = 20$, $\beta_{\text{HO}} = 0$ for all ground-state calculations, and $\beta_{\text{HO}} = 0.4$ for the fission isomer calculations. We also set $N_{\text{Her}} = 40$, $N_{\text{Lag}} = 40$, and $N_{\text{Leg}} = 80$ for the Hermite, Laguerre, and Legendre quadratures, respectively.
- The *physics accuracy* depends on the characteristics of the initial condition used to start the HFB iterations. In HFBTHO, iterations are initialized with the solution of the Schrödinger equation for a Woods-Saxon potential with quadrupole, octupole,

and hexadecapole deformation. In practice, one often specifies only the quadrupole deformation β_2 of the Woods-Saxon potential based on the expected value of the mass quadrupole moment of the nucleus, which we denote Q_t . For a given configuration, parameter point \mathbf{x} , and nucleus (Z, N) , the final quadrupole moment (i.e., at approximate convergence) is denoted by $Q_f \equiv Q_f(Z, N, \mathbf{x})$.

In performing optimization or Bayesian calibration, one may explore a large area of the n_x -dimensional parameter space; there is no guarantee that the HFBTHO program converges for all queried \mathbf{x} . In HFB iteration n , the convergence metric defined as the Euclidean norm $\mu^{(n)} = \|\rho^{(n)} - \rho^{(n-1)}\|_2 = \sqrt{\sum_{ij} [\rho_{ij}^{(n)} - \rho_{ij}^{(n-1)}]^2}$ is a simple filter for accepting the result of the calculation: if $\mu^{(n)} > \varepsilon$ after $n = 500$ iterations, the results are immediately discarded. In this work, we set $\varepsilon = 10^{-5}$.

Even when the calculation passes this filter (i.e., $\mu \leq \varepsilon$), the result may not be physically correct. A first layer of offline postprocessing is thus responsible for flagging as nonsensical those results that have at least one theoretical observable value that is “too far” from physical expectations. Specifically, we flag solutions that have a pairing gap less than -10 keV; a binding energy per nucleon of $E/A < -11$ MeV (either in the ground state or in the fission isomer); or a proton radius r_p outside of the interval $[0.8, 1.1]A^{1/3}$.

A second stage of flagging is applied to those results that have potentially sensible observable values but for which the values are not consistent with the expected characteristics of the configuration of interest. This stage consists mostly of identifying abnormal values of the final quadrupole deformation β_2 . For example, a spherical ground state is flagged if its axial quadrupole deformation has $|\beta_2| > 0.01$; a deformed ground state is flagged unless $0.05 \leq \beta_2 \leq 0.6$; and a fission isomer configuration is flagged unless $0.3 \leq \beta_2 \leq 1.15$. In addition, we require that the fission isomer final deformations be sufficiently larger than the associated ground-state deformation so that a potential barrier can exist between the two states. This requirement is enforced by insisting that all valid results satisfy $\beta_2^{(\text{FI})} > 2.7\beta_2^{(\text{g.s.})}$.

Fission isomers are excited states; therefore their binding energy E_{FI} should exceed that of the associated deformed ground-state $E_{\text{g.s.}}$. While we may allow the fission isomer to be lower than the ground state for some very neutron-rich or superheavy nuclei, our dataset does not contain such exotic systems. Therefore, in addition to tagging fission isomer and deformed ground-state data as nonsensical or nonphysical because of their final deformation, we apply a final layer of outlier analysis. Specifically, a valid fission isomer result that has a valid associated deformed ground-state result is tagged as nonphysical if $E_{\text{FI}} < E_{\text{g.s.}} - 0.5$ MeV.

2.4. The Observable Engine

Each of our studies is defined with respect to a set of n_d observables that are associated with n_{nuc} distinct nuclear configurations; for UNEDF1, $n_{\text{nuc}} = 79$. Our studies require information about how each observable’s theoretical values vary across the parameter

space. For instance, in order to find approximate minimizers of an objective function, optimization software assembles theoretical results of these observables, one parameter space point at a time, to determine the next parameter point for evaluation.

To help acquire and manage such potentially large amounts of data, we developed on top of the HFBTHO solver [43] a layer of software parallelized with MPI, which we call the *observable engine*. This software uses the output of HFBTHO to generate and gather theoretical observable results at each configuration and parameter space point combination contained in the Cartesian product of the n_{nuc} nucleus configurations for a given set of parameter space points. The observable engine also performs online postprocessing of the HFBTHO results to compute all derived theoretical observable values (e.g., fission isomer excitation energies). In the case of optimization, the observable engine is called for each new parameter space point \mathbf{x} . In the case of the Bayesian study reported in Section 4, the observable engine was run on a design \mathcal{D} of D distinct parameter space points, $\mathcal{D} = \{\mathbf{x}_i\}_{i=1,\dots,D}$; in the study in Section 4, we used $D = 500$.

3. Case Study and Impact of Target Quadrupole Moment on Forward Model Calculations and Optimization-Based Inversion

Self-consistent HFB calculations can be unstable with respect to how they are initialized. This problem is relevant for all deformed HFB calculations and is well known by fission practitioners in the calculation of potential energy surfaces (PESs) since it leads to infamous discontinuities [34]. For calibration purposes, these instabilities must be kept tightly under control: in the case of the excitation energy E^* of the fission isomer, for example, one cannot accept that two slightly different values of the quadrupole moment for the initial density lead to significantly different results for E^* . In this work, we focus on the impact of the value Q_t of the quadrupole moment used to drive the self-consistent iterations toward a given solution, either through the determination of the initial deformation or as a constraint imposed on the first few iterations.

Ideally, any ambiguity could be avoided if, for a given nuclear configuration and parameter space point \mathbf{x} , we would estimate the local PES over the range of physically realistic final quadrupole moments, identify all local extrema, and use some physics-based criterion to identify which local minimum is the correct solution. For a study with a large number of configurations and parameter space points, however, this brute-force method rapidly becomes infeasible. In addition, when Lipkin-Nogami corrections are activated (as is the case with the UNEDF1 functional), the self-consistent solution is no longer variational: selected local minima over constrained values of quadrupole moments may not correspond to unconstrained minima.

In the following subsections, we describe a data acquisition, configuration, and analysis scheme that allows one to acquire data without computing local PESs and to determine whether choosing only one out the many possible solutions that HFBTHO can find unduly affects the outcome of the analysis. To this end, we collect the same dataset

Table 1. 95% confidence intervals (CIs) for the UNEDF0, UNEDF1, and UNEDF2 parameterizations; from [9, 10, 13], respectively. When available, the CI is rounded to the nearest integer except for ρ_{sat} , m_s^* , and E^{NM} . The last column defines the volume studied in this work. Note that the CIs for C_t^{JJ} are given only for completeness, since these coupling constants were set to 0 in this work.

Parameter	UNEDF0	UNEDF1	UNEDF2	Interval Studied Here
ρ_{sat}	[0.160, 0.161]	[0.158, 0.159]	[0.154, 0.158]	[0.155, 0.165]
E^{NM}	[−16.1, −16.0]	–	–	[−16.1, −15.5]
K^{NM}	–	–	[223, 257]	[200, 245]
$a_{\text{sym}}^{\text{NM}}$	[26, 36]	[28, 30]	[29, 30]	[28, 32]
$L_{\text{sym}}^{\text{NM}}$	[−21, 111]	[22, 58]	–	[20, 60]
$1/m_s^*$	–	[0.9, 1.5]	[0.8, 1.2]	[0.8, 1.2]
$C_0^{\rho\Delta\rho}$	[−58, −52]	[−53, −37]	[−51, −42]	[−60, −40]
$C_1^{\rho\Delta\rho}$	[−149, 38]	[−218, −73]	[−153, −73]	[−160, −50]
V_0^{n}	[−174, −166]	[−212, −160]	[−223, −195]	[−240, −150]
V_0^{p}	[−205, −194]	[−225, −189]	[−242, −219]	[−265, −180]
$C_0^{\rho\nabla J}$	[−85, −74]	[−81, −67]	[−74, −55]	[−85, −60]
$C_1^{\rho\nabla J}$	[−3, 94]	[−68, −4]	[−64, −13]	[−80, 50]
C_0^{JJ}	–	–	[−82, −24]	[−105, 10]
C_1^{JJ}	–	–	[−95, −36]	[−120, 10]

with multiple Q_t configurations. For a given nuclear configuration computed at a given parameter space point \mathbf{x} , the computation is assumed to be *independent* of Q_t if each of the computations run with a different value of Q_t converges, if all observables are physically reasonable (i.e., not flagged by the rules stated in Section 2.3), and if the results are effectively identical across all target configurations. Because of the lack of variability, such a result would suggest (without proving) that there is a consistent local extremum for the computation within the region of physically relevant final quadrupole moments.

3.1. Parameter Space Volume

The first step is to define the parameter space volume \mathcal{V} , from which all designs \mathcal{D} will be sampled. Our intent was that the parameter space volume \mathcal{V} should allow drawing identical designs for the UNEDF0, UNEDF1, and UNEDF2 protocols. Therefore, the volume was chosen large enough for the statistical analysis to consider parameter values beyond the 95% confidence intervals around each of the previously determined UNEDF0, UNEDF1, and UNEDF2 optimization results but without being so large that one sees many failed HFBTHO computations, nonsensical results, nonphysical results, or results with multiple possible solutions. Note that some of the parameters of the energy functional (e.g., the nuclear incompressibility K^{NM}) are not very sensitive to ground-state properties and are therefore ill-constrained: their most likely value determined by the statistical calibration may be at the boundaries of the volume considered.

Table 1 shows the intervals (last column) used to define \mathcal{V} and compares them

with the 95% confidence intervals (CIs) for each of the three UNEDF parameterizations. For the six coupling constants related to the surface, spin orbit, and tensor terms of the Skyrme functional and the two coupling constants of the pairing functional, the proposed interval encompasses all three CIs (with the exception of $C_1^{\rho\nabla J}$ for UNEDF0). For the nuclear matter properties, physics constraints sometimes impose tighter bounds than what the result of the statistical analysis may have suggested.

3.2. Self-Consistent Determination of Configurations for Deformed Nuclei

For simplicity, we assume that for a given nuclear configuration we can use the same target quadrupole moment across all parameter space points \mathbf{x} in the design \mathcal{D} . For example, in the case of spherical ground-state nuclei, we adopt the accepted approach of setting $Q_t(\mathbf{x}) = 0$ b for all \mathbf{x} in the design. Note, however, that the constant value of Q_t can be different for each nuclear configuration.

Given a volume \mathcal{V} of the parameter space, we would like to determine for each deformed configuration a Q_t value that is both motivated by experimental results and representative of the final deformations for that configuration across the entire volume. To this end, we devised a self-consistent, iterative scheme with initial target values, $Q_t^{(0)}$, set by physical expectations. Specifically, for each deformed ground state, we adopted an initial quadrupole moment that is consistent with an axial quadrupole deformation $\beta_2 = 0.3$; in the case of fission isomers, the same configuration scheme is adopted but with the experimentally motivated initial quadrupole moment set to the value consistent with $\beta_2 = 0.6$.

Given a design \mathcal{D} of points \mathbf{x} contained in the volume of interest in the functional's parameter space, the procedure is as follows. For each configuration in the study, the final values of the quadrupole moment $Q_f^{(i)}(\mathbf{x})$ at iteration i are used to configure the observable engine at iteration $i + 1$. Specifically, for all points \mathbf{x} in the design \mathcal{D} , we set $Q_t^{(i+1)}$ to the median of the final quadrupole moment values obtained for that state across all points \mathbf{x} in the design at the previous iteration: $Q_t^{(i+1)} = \langle Q_f^{(i)}(\mathbf{x}) \rangle_{\mathcal{D}}$. A result is included in the computation of the median only if it was convergent and if postprocessing determined that the result is both sensible and physically reasonable. This iterative procedure stops when no Q_t values change appreciably for two successive iterations. For UNEDF1, convergence was reached in four such iterations with a maximum change in Q_t of approximately 0.05 b; see Table 2. We refer to this initial Q_t configuration as \mathcal{C}_0 .

To search for other possible HFBTHO solutions, we derived two other Q_t configurations, \mathcal{C}_1 and \mathcal{C}_2 , directly from the results used to determine \mathcal{C}_0 . For \mathcal{C}_1 , the target configuration for each state was set to the 12.5 percentile of the Q_f values for \mathcal{C}_0 ; for \mathcal{C}_2 , it was set at the 87.5 percentile. These values are different enough to increase the likelihood of finding other local extrema but close enough to avoid finding solutions with final deformation too far from physically motivated expectations.

Table 2. Results of the self-consistent adjustment of the target quadrupole moment Q_t for deformed nuclei. The first four rows correspond to the iterations of the initial configuration \mathcal{C}_0 ; the last two rows show the final results for two other configurations; see text for details. Column 2 shows the maximum difference between the target and final quadrupole moment across all nuclear configurations; columns 3 and 5 are the percentage of nonconvergent and nonphysical computations out of total 39,500 computations in the design, respectively; column 4 is the number of nonsensical computations.

Config.	$\max(\Delta Q_f)$ [b]	Nonconv.	Nonsens.	Nonphys.
$\mathcal{C}_0^{(0)}$	33.279	1.87%	1	4.84%
$\mathcal{C}_0^{(1)}$	1.767	1.20%	1	0.90%
$\mathcal{C}_0^{(2)}$	0.508	1.12%	1	0.92%
$\mathcal{C}_0^{(3)}$	0.051	1.13%	1	0.93%
\mathcal{C}_1	—	1.76%	0	0.90%
\mathcal{C}_2	—	1.62%	1	0.96%

3.3. Analysis of Acquired Data and Dependence on Q_t

The results of the self-consistent determination of the target quadrupole moment configuration \mathcal{C}_0 are displayed in Table 2. We can clearly see that the first iteration, which stepped the configuration away from one motivated purely by experimental expectations, was successful in decreasing the number of failed computations in the design. However, the table shows that even for the final datasets, the number of nonconvergent computations and results with nonsensical or nonphysical results is nonzero. We also note that for all three configurations the number of parameter space points with at least one unacceptable result is about half the total number of points in the design. In other words, for an arbitrary \mathbf{x} point in the design, there is an approximately 50% chance that at least one of the 79 HFB calculations needed to define the value of the objective function (2) has failed. These failures seem unavoidable and introduce an effective “noise” in the objective function. We show later that this noise has insignificant impact on the optimization and calibration.

The histograms in Figure 1 show that there is a region of the parameter space volume in which invalid results are generated regardless of the target quadrupole configuration used. There is also a second region in which the binding energy of the fission isomer is significantly outside the range of allowed values, for example, quite lower than the ground state. Therefore, the failure statistics for the design \mathcal{D} could be significantly improved if such regions were excluded; we note, however, that some failures would continue to be unavoidable even with such filtering.

Each combination of nuclear configuration and parameter space point in the design was classified based on how many of the \mathcal{C}_0 , \mathcal{C}_1 , and \mathcal{C}_2 computations failed and whether the valid results were independent of the Q_t value used. For spherical ground-state computations, we found that the difference in Q_f that arises from using different Q_t is small overall, almost always less than 0.1 b. Therefore, we deem them Q_t -dependent

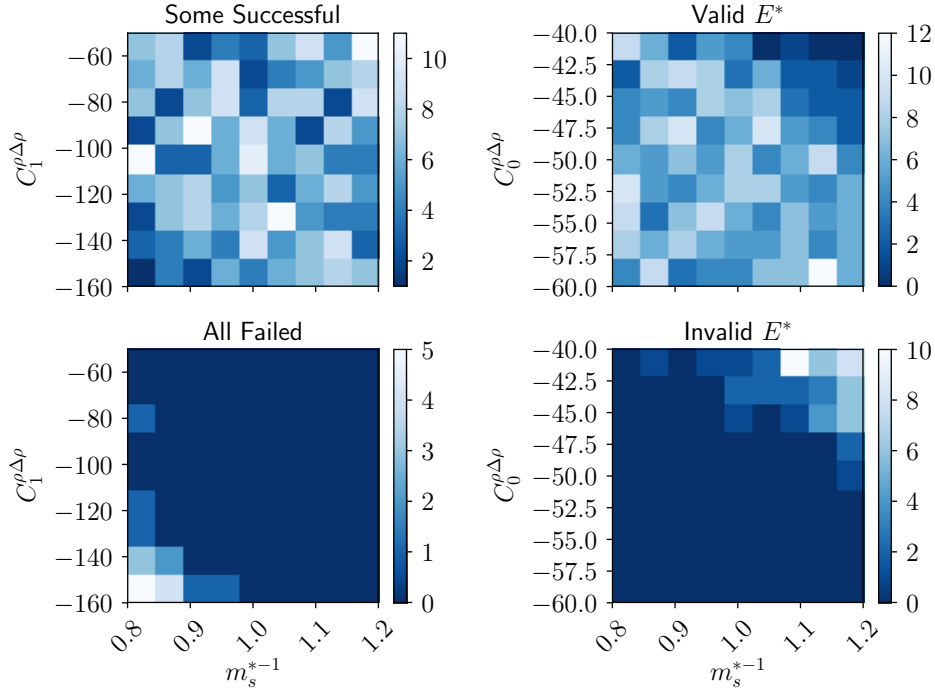


Figure 1. Two-dimensional histograms showing the number of failures in a two-dimensional projection of the n_x -dimensional space. Left column: failure counts for ground-state binding energies, proton radii, and OES staggering in the $(1/m_s^*, C_1^{\rho\Delta\rho})$ plane. The label “All Failed” indicates that at least 3 different nuclear configurations had unacceptable results for all configurations C_0, C_1 , and C_2 . Right column: failure counts for fission isomer excitation energy in the $(1/m_s^*, C_0^{\rho\Delta\rho})$ plane. The label “Invalid E^* ” indicates that at least 2 fission isomers were flagged.

if the maximal difference in binding energy between valid computations exceeds 0.002 MeV. For deformed ground state or fission isomer computations, the Q_f value for some of the outliers can change by up to 10 b. The computation is thus classified as Q_t -dependent if the maximal difference in Q_f exceeds 0.5 b.

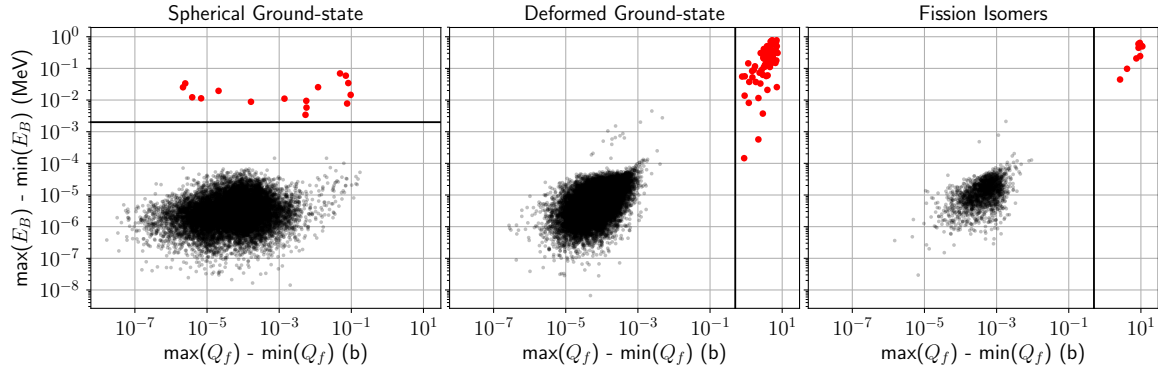


Figure 2. Spread in energy plotted as a function of the spread in final quadrupole moments across the three Q_t configurations discussed in Section 3.2.

Figure 2 gives a visual representation of this analysis. For the spherical and deformed ground-state energies, as well as for the fission isomers, we recorded the spread in energy and final quadrupole moments across the three Q_t configurations described in Section 3.2 when at least two of the C_0, C_1, C_2 results were convergent, sensible, and physical. The spread values were computed only across those results that were convergent, sensible, and physical. The figure shows the spread in energy as a function of the spread in final quadrupole moment for these three observables. Most of the computations are characterized by a very small spread of a few dozen eV for the energy and on the order of millibarns for the quadrupole moments. The outliers, marked in red and separated from the rest by a line, are easily identified. Note that deviations can reach up to 1 MeV for the energy, which will introduce a larger contribution to the objective function (2). The configurations with greater Q_t dependence are often those with many nonconvergent computations. The main conclusion of this analysis is that the parameter space volume was indeed small enough that the number of Q_t -dependent results was relatively small.

3.4. Effect on the Parameter Optimization

To study the effect of Q_t configurations on optimization, we attempted to reproduce the original UNEDF1 optimization result reported in [10]. Four optimizations, each using a different Q_t configuration, were run for 350 \mathbf{x} evaluations; the POUNDERS optimization software from [45] drove HFBTHO via the observable engine. These runs were set up such that each HFBTHO computation used the default HFBTHO initial state corresponding to the given nuclear configuration and Q_t value. As with the original UNEDF1 optimization, all optimization runs started from the UNEDF0 parameter values and used the same bound constraints as those in [10].

As seen in Table 3, the parameterizations found from these four optimization runs are consistent with the original UNEDF1 optimization results. However, while K^{NM} was actively constrained at its lower bound in the original study, this is not the case (although sometimes K^{NM} was barely constrained) for any of the new parameterizations. Future studies could include new UNEDF1 optimizations run with relaxed bound constraints on parameters such as E^{NM} and K^{NM} (e.g., using the intervals that define the parameter space volume used in this study; see Table 1).

Since our optimizations run without the benefit of the offline postprocessing flagging of results mentioned in Section 2.3, the trajectories of the optimization can potentially be affected by nonconvergent or nonphysical results. The failure statistics provided in Table 3 were collected only after the optimizations finished and indicate that the optimizations were robust to nonconvergent HFBTHO computations. The majority of these failures occurred for the (92, 146) fission isomer and only after the χ^2 value had decreased to a value close to the best one reported here. An investigation of these failed computations revealed that HFBTHO was finding two possible solutions: the first was near an inflection point in the PES rather than an extremum (refer to Section 3), and

Table 3. History of UNEDF1 optimizations. The columns correspond to the parameter optimization constraints, the original UNEDF1 parameterization reported in Table II of [10], the standard deviations also reported in Table II of [10], and the parameterizations found by using the Q_t configurations defined here. The final four rows are the number of nonconvergent, nonsensical, and nonphysical computations out of the total 27,650 computations in each optimization, as well as the number of parameter space points with at least one nuclear configuration whose computation was nonconvergent or yielded nonsensical or nonphysical results. The parameter values in bold indicate that the associated parameter was actively constrained by the bounds.

	Bounds	UNEDF1	σ	\mathcal{C}_0	\mathcal{C}_1	\mathcal{C}_2	\mathcal{C}_0^*
ρ_{sat}	[0.15, 0.17]	0.15871	0.00042	0.15850	0.15879	0.15881	0.15876
E^{NM}	[-16.2, -15.8]	-15.8	—	-15.8	-15.8	-15.8	-15.8
K^{NM}	[220, 260]	220	—	222.416	220.000	220.156	220.340
$a_{\text{sym}}^{\text{NM}}$	[28, 36]	28.987	0.604	29.010	29.041	29.048	29.047
$L_{\text{sym}}^{\text{NM}}$	[40, 100]	40.005	13.136	40.599	40.000	40.000	40.042
m_s^*	[0.9, 1.5]	0.992	0.123	0.976	0.981	0.996	0.978
$C_0^{\rho\Delta\rho}$	$(-\infty, \infty)$	-45.135	5.361	-44.064	-44.636	-45.131	-44.370
$C_1^{\rho\Delta\rho}$	$(-\infty, \infty)$	-145.382	52.169	-140.159	-136.479	-136.506	-136.847
V_0^n	$(-\infty, \infty)$	-186.065	18.516	-183.378	-184.055	-186.303	-183.688
V_0^p	$(-\infty, \infty)$	-206.580	13.049	-204.971	-205.605	-207.136	-205.146
$C_0^{\rho\nabla J}$	$(-\infty, \infty)$	-74.026	5.048	-73.007	-73.585	-73.663	-73.193
$C_1^{\rho\nabla J}$	$(-\infty, \infty)$	-35.658	23.147	-28.553	-28.431	-32.673	-30.990
χ^2	—	52.201	—	51.942	51.920	51.967	51.890
Nonconv.	—	—	—	306	405	421	30
Nonsens.	—	—	—	0	0	0	0
Nonphys.	—	—	—	2	0	0	0
Failures	—	—	—	290	283	313	28

the second was at the neighboring local PES maximum. It appears that computations tending toward the PES maximum have a much harder time converging within HFBTHO.

To see whether an alternative initial state setup scheme would yield “cleaner” results, we used the fourth configuration \mathcal{C}_0^* . The only difference between \mathcal{C}_0^* and \mathcal{C}_0 is the scheme used for setting the initial state for each HFBTHO computation. Specifically, for each nuclear configuration in the optimization protocol, the first computation was run using the same default HFBTHO initial state mentioned above. For all subsequent computations, however, the initial state was set using the solution for the same nuclear configuration from the previous parameter space point. Although this optimization run encountered far fewer nonconvergent computations, the parameterization obtained was not changed significantly. The setup scheme of \mathcal{C}_0 should be preferable to that of \mathcal{C}_0^* since the solution of the latter has a potentially stronger dependence on the initial starting point in parameter space as well as the default initial state. That said, the fact that this optimization also settles in the same region of the parameter space as the others bolsters the case that POUNDERS appears to find a consistent approximate local minimum for this objective function.

4. Statistical Emulation and Calibration

Bayesian inference has become common in the nuclear physics community for quantification of uncertainties [46, 47, 48, 49, 50, 51, 52, 53, 54, 55, 56]. The goal of Bayesian inference here is to estimate a distribution of UNEDF1 parameters that probabilistically match experimental observations, which are assumed to have been measured with error. To do so, we construct a Bayesian model that has two components. The *likelihood*, $f(y|\mathbf{x})$, is our distribution for the experimental observations y given the unknowns (i.e., the UNEDF1 parameters \mathbf{x}). The *prior*, $\pi(\mathbf{x})$, is a marginal distribution for the unknown parameters that summarizes our knowledge of these parameters before observing data. Following the rules of probability, one can construct the posterior distribution of the unknown UNEDF1 parameters given the observations as

$$p(\mathbf{x}|y) \propto \pi(\mathbf{x})f(y|\mathbf{x}).$$

One of the key ideas is that the likelihood $f(y|\mathbf{x})$ is based on forward evaluations of the UNEDF1 objective function in (2).

For complicated Bayesian models, the posterior distribution cannot be directly integrated to obtain moments, and the normalization term cannot be directly integrated to remove the proportionality. Instead, Markov chain Monte Carlo (MCMC) is typically used to draw samples from the posterior distribution. MCMC is a sequential sampling method that requires forward evaluations only of the unnormalized posterior distribution. For details on MCMC methods, see [57].

4.1. Statistical Emulation and Calibration of UNEDF1

Statistical quantities expressible as expectations calculated by using the posterior samples will approximate the full posterior quantities with a well-understood approximation error that shrinks as the number of MCMC samples increase. MCMC methods are desirable approximations to the full posterior for this reason; however, they require a large number of evaluations of the likelihood for each evaluated parameter value. Because of high correlation among some UNEDF1 parameters, more than 1 million samples would be required in order to get a reasonable estimation of posterior quantities. That would require millions of evaluations of UNEDF1 for all experimental observables, which is an infeasible computational cost.

In order to overcome this computational bottleneck, the evaluation of UNEDF1 in the MCMC process is replaced by a computationally inexpensive emulator. In principle, any fast regression or function approximation technique can be used as an emulator of UNEDF1. Gaussian processes have been used as emulators for many years across many fields, largely because of two main advantages of GP emulators. First, GPs interpolate the observed values at the locations where the computer model has been evaluated, properly reflecting the information about the response of the computer model at that location. Second, GPs not only give flexible, accurate predictions but also provide an

estimate of uncertainty in predictions from the emulator at locations where the model has not been evaluated. Thus, GPs allow calibration and prediction to properly account for limited evaluations of a computer model such as UNEDF1.

A GP is a stochastic process indexed by a n_x -dimensional input space where any finite collection of random variables in the process are multivariate normally distributed [58]. The process defines a prior distribution on functions of the input space,

$$f(\mathbf{x}) \sim \mathcal{N}(\mu(\mathbf{x}), k(\mathbf{x}, \mathbf{x}', \boldsymbol{\kappa})), \quad (3)$$

where \mathcal{N} denotes a (multivariate) Gaussian distribution, $\mu(\mathbf{x})$ is the mean function of the process, $k(\mathbf{x}, \mathbf{x}', \boldsymbol{\kappa})$ is a function that gives the covariance between function outputs at two locations in input space, and $\boldsymbol{\kappa}$ is a vector of hyperparameters for the covariance function (e.g., correlation length). A common covariance function is the squared exponential function

$$k(\mathbf{x}, \mathbf{x}', \boldsymbol{\kappa}) = \sigma e^{-\frac{(\mathbf{x}-\mathbf{x}')^2}{\ell^2}},$$

where $\boldsymbol{\kappa} = (\sigma, \ell)$ with σ the marginal variance of the process, which defines the scales over which functions in the function space are expected to vary, and ℓ is the correlation length of the GP. The choice of covariance function and its hyperparameters dictates the properties of the prior distribution on functions and the type of function space supported [58]. The entry in the i^{th} row and j^{th} column of the correlation matrix between outputs of $f(\mathbf{x})$ at a finite set of locations in the input space is the correlation function evaluated at \mathbf{x}_i and \mathbf{x}_j , $k(\mathbf{x}_i, \mathbf{x}_j, \boldsymbol{\kappa})$.

After defining the GP prior, the GP is updated by using Gaussian conditioning on a set of evaluations of the computer model, $\mathbf{f} = [f(\mathbf{x}_1), \dots, f(\mathbf{x}_D)]$. The GP at a set of new locations, \mathbf{x}^* , conditioned on observation of \mathbf{f} , that is,

$$f(\mathbf{x}^*) \mid \mathbf{f} \sim \mathcal{N}\left(\tilde{\mu}(\mathbf{x}^*), \tilde{\Sigma}(\mathbf{x}^*, \mathbf{x}^*)\right),$$

has a posterior mean and covariance matrix of

$$\begin{aligned} \tilde{\mu}(\mathbf{x}^*) &= \mu(\mathbf{x}^*) + \Sigma(\mathbf{x}^*, \mathbf{x})\Sigma(\mathbf{x}, \mathbf{x})^{-1}(\mathbf{f} - \mu(\mathbf{x})), \\ \tilde{\Sigma}(\mathbf{x}^*, \mathbf{x}^*) &= \Sigma(\mathbf{x}^*, \mathbf{x}^*) - \Sigma(\mathbf{x}^*, \mathbf{x})\Sigma(\mathbf{x}, \mathbf{x})^{-1}\Sigma(\mathbf{x}, \mathbf{x}^*), \end{aligned}$$

where $\Sigma(\mathbf{x}, \mathbf{x})$ is the $D \times D$ covariance matrix with entry i, j equal to $k(\mathbf{x}_i, \mathbf{x}_j, \boldsymbol{\kappa})$. The $\boldsymbol{\kappa}$ -dependence in Σ has been suppressed for clarity. $\Sigma(\mathbf{x}^*, \mathbf{x})$ represents the $n_{\text{new}} \times D$ cross-covariance terms between outputs at the n_{new} locations to be predicted by $f(\mathbf{x}^*)$ and observed locations of the function $f(\mathbf{x})$. The posterior mean, $\tilde{\mu}(\mathbf{x}^*)$, is recognized as an accurate emulator of many complex physical models [59, 60, 61, 62]. The posterior variance represents uncertainty in the output of the function at a location where it has not yet been evaluated. Inclusion of this uncertainty, rather than using a point-estimate prediction, allows for uncertainty in a function at unevaluated points to be reflected in the uncertainty associated with estimating \mathbf{x} .

For the emulation of UNEDF1 in this work, the function (or computer model) is the objective function (2). This function was evaluated at $D = 500$ locations in the

12-dimensional volume \mathcal{V} listed in Table 1. These locations form the design \mathcal{D} and were determined by a maximin, space-filling Latin hypercube design using the R package `lhs` [63]. The choice of 500 evaluations was determined by balancing estimates of emulation error using cross-validation with computational cost of larger sample size for building the emulator.

Typically, during the calibration and emulation process, the GP hyperparameters are included in the sampling in order to fully account for their uncertainty in the calibration process. Their inclusion requires that the GP covariance matrix across observations be rebuilt and inverted many times, which can add substantial cost to the sampling process—the memory requirement to store the covariance matrix scales as $\mathcal{O}(D^2)$ and the computational cost to invert scales as $\mathcal{O}(D^3)$ —and have minor effect on the posterior distribution for the calibration parameters of interest [64]. Instead, we follow the modularization approach of Liu et al. [64] and fix the hyperparameters to a point estimate—specifically to the maximum likelihood estimate using the `scikit-learn` GP implementation [65]. Full sampling via MCMC of all parameters in the Bayesian model was carried out for 25,000 samples and showed posterior estimates consistent with the modularization approach. Despite two weeks of computational time to collect those samples, however, the Markov chains for the full Bayesian model were poorly converged and thus not used in this work.

For emulation of (2), the input space for the GP can be defined both on the parameters of the model \mathbf{x} and on the physical inputs $\boldsymbol{\nu}$ such as proton number Z and neutron number N . In other words, we may write the objective function as $f(\mathbf{x}, \boldsymbol{\nu})$. Because HFBTHO is run at all values of $\boldsymbol{\nu}$ for each \mathbf{x} , however, the number of total observations would be $D \times n_d$, which can be computationally infeasible. Instead, we can treat the vector of values, $[f(\mathbf{x}, \nu_1), \dots, f(\mathbf{x}, \nu_{n_d})]$ as a multivariate output of HFBTHO rather than n_d scalar outputs. The evaluations of HFBTHO can then be stacked into the $D \times n_d$ matrix \mathbf{M} .

To do so, we follow the approach presented in [62, 47], using principal component analysis (PCA) to define a number of empirical basis functions capturing the variation in the HFBTHO output across $\boldsymbol{\nu}$. Using $n_b \ll n_d$ PCA bases, we can reconstruct the vector of HFBTHO outputs across $\boldsymbol{\nu}$ as

$$[m(\boldsymbol{\nu}_1, \mathbf{x}_i), \dots, m(\boldsymbol{\nu}_{n_d}, \mathbf{x}_i)] = \boldsymbol{\mu} + \mathbf{S} \sum_{j=1}^{n_b} \mathbf{k}_j w_j(\mathbf{x}_i) = \boldsymbol{\mu} + \mathbf{SK}\mathbf{w},$$

where \mathbf{K} is a matrix made up of the PCA basis vectors \mathbf{k}_j and \mathbf{w} is the vector of PCA weights $w_j(\mathbf{x}_i)$ as a function of the parameters \mathbf{x} . $\boldsymbol{\mu}$ is the n_d -length vector of the mean of the columns of \mathbf{M} . \mathbf{S} is an $n_d \times n_d$ diagonal matrix of the empirical standard deviations of the same. For this study, twelve PCA basis functions are used to capture 99.97% of the variability of the output across $\boldsymbol{\nu}$. The weights, $w_j(\mathbf{x}_i)$, can each be modeled with a GP.

The resulting likelihood, given a parameter vector $\hat{\mathbf{x}}$, is

$$y \mid \hat{\mathbf{x}} \sim \mathcal{N} \left(\mathbf{SK}\tilde{\boldsymbol{\mu}}(\hat{\mathbf{x}}) + \boldsymbol{\mu}, \mathbf{SK}\tilde{\boldsymbol{\Sigma}}(\hat{\mathbf{x}}, \hat{\mathbf{x}})\mathbf{K}^T\mathbf{S} + \boldsymbol{\Lambda}\boldsymbol{\Sigma}_\epsilon \right),$$

where Σ_ϵ is the diagonal matrix capturing the given measurement error and PCA truncation error. Experimental measurement error has been provided with the observed data; however, a scaling matrix Λ is introduced to allow the data to inform the precision with which the UNEDF1 model can capture variation in the experimental observations. Following [47], we estimate a multiplicative scaling factor λ_j on the given standard deviation σ_i of the measurement error for each of the six data types: spherical nuclei binding energy, deformed nuclei binding energy, proton r.m.s. radii, proton pairing gap, neutron pairing gap, and excitation energy of fission isomers. The i^{th} diagonal entry of Λ corresponds to the λ_j for the data type of y_i .

Given this specification of the likelihood, the prior distributions for both the UNEDF1 parameters \mathbf{x} and scaling factors λ_j are needed in order to complete the statistical model. For \mathbf{x} , upper and lower bounds on physically plausible values in Table 1 define the support of the prior distributions. Within these bounds, the prior distribution was determined to be uniform to express the assumption that all plausible values were equivalently likely a priori. Each scale parameter λ_j was assigned a Gamma prior distribution, $\lambda_j \sim \Gamma(\alpha, \beta)$ with $\alpha = \beta = 5$, reflecting the prior expectation that the multiplicative scale should be near $\frac{\alpha}{\beta} = 1$, but with a prior standard deviation of $\frac{\sqrt{5}}{5}$, allowing reasonable variation near 1. As stated before, the GP hyperparameters were estimated from the simulation results alone and then fixed.

To fit the Bayesian model, we obtain samples from the posterior distribution using the “No-U-turn” variant of Hamiltonian Monte Carlo implemented in the Stan probabilistic programming language [66]. Four chains of 1,500 samples each were obtained, and convergence of the chains to the target posterior distribution was confirmed by using the \hat{R} diagnostic [66, 67].

4.2. Impact of Changing Q_t Target on Calibration of UNEDF1

The statistical model described in Sec. 4.1 was fit with both the full set of 500 evaluations of UNEDF1 and a truncated set removing runs with at least one unacceptable value as described in Sec. 3.3. This resulted in 279, 238, and 244 out of 500 runs included in the truncated set for $\mathcal{C}_0, \mathcal{C}_1$, and \mathcal{C}_2 , respectively.

Comparison of the posterior distribution for the parameters \mathbf{x} shows little evident sensitivity to the differing Q_t values for either the full or truncated case. The diagonal and lower triangle of panels in Figure 3 show posterior summaries from the three Q_t configurations $\mathcal{C}_0, \mathcal{C}_1$, and \mathcal{C}_2 for the full and truncated models, with the color indicating the Q_t configuration. For a fixed color, the bright curve indicates the truncated data and the muted curve indicates the full set. The diagonal panels show density estimates of the 1D marginal distributions for each of the 12 parameters, while the lower triangle of panels shows 90% credible regions for the 2D joint marginal distributions. For both the 1D and 2D marginals, the plots show extremely high agreement across configurations, indicating little effect of changing the Q_t . This can also be quantified by using the MCMC \hat{R} diagnostic [67]: values close to 1 for \hat{R} indicate that the results are consistent

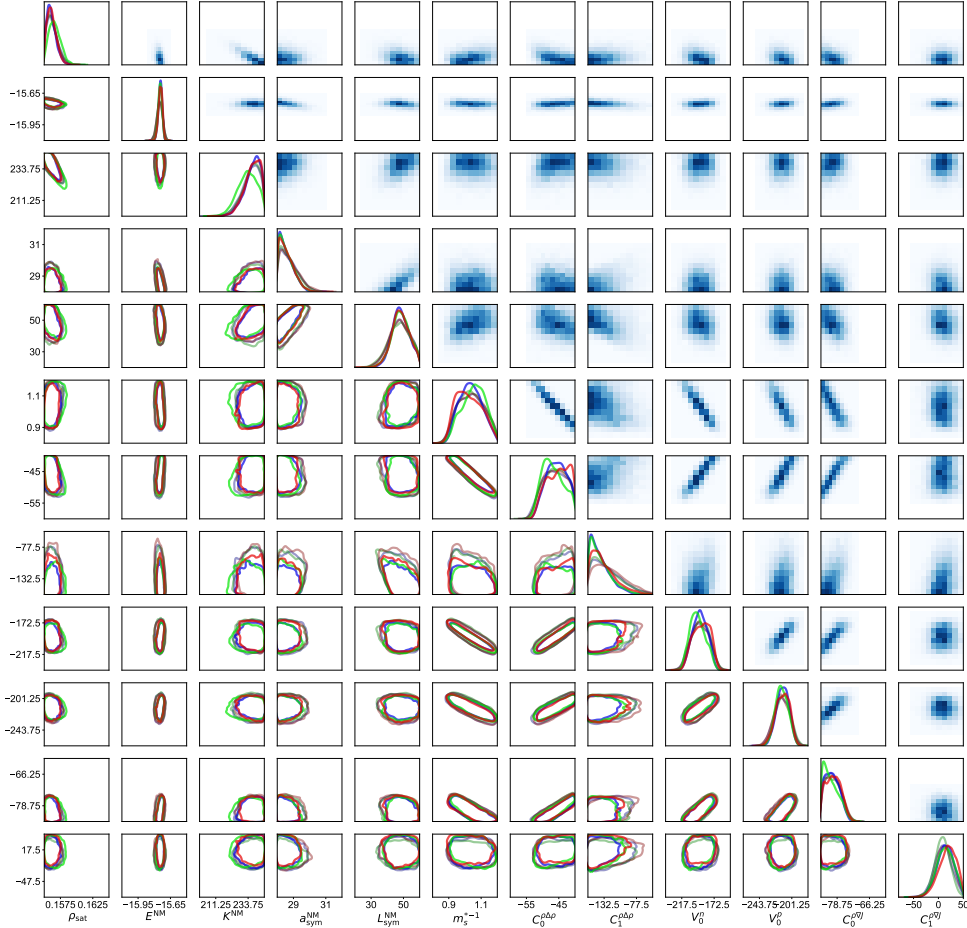


Figure 3. Bivariate and univariate posterior summaries for the calibration parameters. The diagonal shows the estimated 1D marginal posterior densities for the three configurations C_0, C_1 , and C_2 with the muted color fit to the full UNEDF1 data set and the bright color fit removing runs with unacceptable observations (according to the definition from Section 3.3). The lower triangle compares 2D joint 90% credible regions. The upper triangle shows 2D histograms for the 2D joint marginal distribution for C_0 to illustrate the structure of the highest posterior probability region.

with being one set of samples originating from the same target distribution [67]. The maximum \hat{R} across all model parameters comparing chains from the three full and truncated data cases were 1.0086 and 1.062 respectively, well below the recommended threshold deviation from 1 of 1.1000 [66]. The full and truncated results give consistent calibration in Figure 3, with the truncated data leading to slightly more concentrated posterior density for $a_{\text{sym}}^{\text{NM}}$, $L_{\text{sym}}^{\text{NM}}$, and $C_1^{\rho\Delta\rho}$.

Table 4. Posterior mean and 95% credible interval for each of the 6 *a priori* theoretical errors σ_i in (2). The Bayesian model shows strong evidence that the data are consistent with a standard deviation much smaller than that expected *a priori* for the deformed nuclei binding energies, and with a slightly larger than expected standard deviation for the fission isomer excitation energy.

Posterior estimates for σ_i			
Data type	Mean	95% credible interval	Default
E_{sph} [MeV]	1.9500	[1.7300, 2.6300]	2.00
E_{def} [MeV]	0.2270	[0.2060, 0.2930]	2.00
Δ_n [MeV]	0.0457	[0.0337, 0.0857]	0.05
Δ_p [MeV]	0.0703	[0.0570, 0.1120]	0.05
r_p [fm]	0.0177	[0.0159, 0.0235]	0.02
E_{FI}^* [MeV]	0.8500	[0.7050, 1.3290]	0.50

The upper triangle of panels in Figure 3 shows 2D histograms of the joint marginal distributions across parameters \mathbf{x} for \mathcal{C}_0 . Several parameters show strong pairwise correlations in the posterior distributions: m_s^* , $C_0^{\rho\Delta\rho}$, V_0^n , V_0^p , and $C_0^{\rho\nabla J}$. The strong correlation is indicative of the parameter values being only weakly identifiable from current data. Targeted measurements to disentangle these correlations could substantially decrease the uncertainty of all five parameters. Two other parameters, ρ_{sat} and K^{NM} , show similar high correlation. Because the posterior distribution is concentrated against the boundary of the *a priori* feasible region, there is some evidence that combinations of ρ_{sat} and K^{NM} may be consistent with the data that were ruled out when choosing parameter ranges. This is also true of $C_0^{\rho\Delta\rho}$, although $C_0^{\rho\Delta\rho}$ still has large uncertainty relative to the scale of the prior range when compared with other parameters.

In addition to the calibration of \mathbf{x} , the scale σ_i of the *a priori* theoretical error was also informed by the data; see (2). Table 4 shows the posterior mean and 95% credible region for each of the six data types for Bayesian model with the full data. The posterior distribution for the standard deviation of binding energy for deformed nuclei was much smaller than assumed, indicating that the data were less variable and more informative for \mathbf{x} than thought *a priori*. Conversely, the standard deviation for fission isomer excitation energy was slightly larger, indicating more variable observed quantities than previously expected. The estimated scale with the truncated data was consistent with Table 4 and was omitted for brevity.

5. Conclusion

In this paper, we presented a comprehensive procedure to optimize and calibrate nuclear energy density functionals when deformed nuclei are included in the data. We paid special attention to the initialization of the self-consistent calculations, which can have unwelcome impact on the characteristics of the HFB solution. While our case study

was based on the UNEDF1 Skyrme functional, our results could easily be applied to the calibration of other types of energy functionals. Our analysis leads to the following conclusions: (i) Embedding diagnostic tools in the optimization/calibration process is especially important to avoid regions of the parameter space that lead to nonphysical solutions and to minimize the amount of “noise” in the computed quantities such as the objective function (2). (ii) Owing to the nonlinearity of the HFB equations, some calculations will always fail one way or the other during the optimization; but if the initial parameter space volume has been well set up, our diagnostic tools show that these failures will not dramatically impact the final parameterizations. (iii) Bayesian calibration and direct optimization give similar, robust (e.g., to the initializations considered and code/dependency/compiler changes over the past several years) results. (iv) By treating the a priori errors of each data type as hyperparameters, Bayesian calibration can provide narrower estimates of these errors. In the case of the UNEDF1 functional, the estimate for the standard error for deformed nuclei turned out to be 10 times smaller than expected.

Our estimate of theoretical error lend additional credence to the commonly accepted view that deformed nuclei can be well described at the HFB approximation. The fact that the standard error for spherical nuclei is about 10 times larger than that for deformed nuclei also suggests that beyond-mean-field corrections are needed to improve the overall quality of the fit [32]. As noted in [13], some of the parameters of the Skyrme functional cannot be properly constrained by the existing data and/or the limitations of the HFB approximation. Although changes in the initialization configurations of the calibration did not change the values of the coupling constants “much,” the effect of these changes on physics predictions needs to be tested on a case-by-case basis.

Acknowledgments

This work was supported by the U.S. Department of Energy, Office of Science, Offices of Advanced Scientific Computing Research and Nuclear Physics SciDAC programs under Contract numbers DE-AC02-06CH11357 (Argonne) and 89233218CNA000001 (Los Alamos), and by the NUCLEI SciDAC project. It was partly performed under the auspices of the US Department of Energy by the Lawrence Livermore National Laboratory under Contract DE-AC52-07NA27344. We gratefully acknowledge the computing resources provided by the Laboratory Computing Resource Center at Argonne National Laboratory and by the Lawrence Livermore National Laboratory Institutional Computing Grand Challenge program.

Bibliography

- [1] The DOE NSAC Committee. The 2015 Long-Range Plan for Nuclear Science. Technical report, U.S. Department of Energy, 2015.
- [2] M. R. Mumpower, R. Surman, G. C. McLaughlin, and A. Aprahamian. The impact of individual nuclear properties on r-process nucleosynthesis. *Prog. Part. Nucl. Phys.*, 86:86, 2016.

- [3] S. A. Giuliani, Z. Matheson, W. Nazarewicz, E. Olsen, P.-G. Reinhard, J. Sadhukhan, B. Schuetrumpf, N. Schunck, and P. Schwerdtfeger. Colloquium: Superheavy elements: Oganesson and beyond. *Rev. Mod. Phys.*, 91(1):011001, 2019.
- [4] J. Engel, M. Bender, J. Dobaczewski, J. H. de Jesus, and P. Olbratowski. Time-reversal violating Schiff moment of ^{225}Ra . *Phys. Rev. C*, 68(2):025501, 2003.
- [5] J. Dobaczewski and J. Engel. Nuclear Time-Reversal Violation and the Schiff Moment of Ra^{225} . *Phys. Rev. Lett.*, 94(23):232502, 2005.
- [6] Nicolas Schunck. *Energy Density Functional Methods for Atomic Nuclei*. IOP Expanding Physics. IOP Publishing, Bristol, UK, 2019. OCLC: 1034572493.
- [7] T. Nikšić, D. Vretenar, and P. Ring. Relativistic nuclear energy density functionals: Adjusting parameters to binding energies. *Phys. Rev. C*, 78(3):034318, 2008.
- [8] P. Klüpfel, P.-G. Reinhard, T. J. Bürvenich, and J. A. Maruhn. Variations on a theme by Skyrme: A systematic study of adjustments of model parameters. *Phys. Rev. C*, 79(3):034310, 2009.
- [9] M. Kortelainen, T. Lesinski, J. Moré, W. Nazarewicz, J. Sarich, N. Schunck, M. V. Stoitsov, and S. Wild. Nuclear energy density optimization. *Phys. Rev. C*, 82(2):024313, 2010.
- [10] M. Kortelainen, J. McDonnell, W. Nazarewicz, P.-G. Reinhard, J. Sarich, N. Schunck, M. V. Stoitsov, and S. M. Wild. Nuclear energy density optimization: Large deformations. *Phys. Rev. C*, 85(2):024304, 2012.
- [11] J. Erler, C. J. Horowitz, W. Nazarewicz, M. Rafalski, and P.-G. Reinhard. Energy density functional for nuclei and neutron stars. *Phys. Rev. C*, 87(4):044320, 2013.
- [12] Wei-Chia Chen and J. Piekarewicz. Building relativistic mean field models for finite nuclei and neutron stars. *Phys. Rev. C*, 90(4):044305, 2014.
- [13] M. Kortelainen, J. McDonnell, W. Nazarewicz, E. Olsen, P.-G. Reinhard, J. Sarich, N. Schunck, S. M. Wild, D. Davesne, J. Erler, and A. Pastore. Nuclear energy density optimization: Shell structure. *Phys. Rev. C*, 89(5):054314, 2014.
- [14] R. Navarro Pérez, N. Schunck, A. Dyhdalo, R. J. Furnstahl, and S. K. Bogner. Microscopically based energy density functionals for nuclei using the density matrix expansion. II. Full optimization and validation. *Phys. Rev. C*, 97(5):054304, 2018.
- [15] J. Dobaczewski, W. Nazarewicz, and P.-G. Reinhard. Error Estimates of Theoretical Models: A Guide. *J. Phys. G: Nucl. Part. Phys.*, 41:074001, 2014.
- [16] N. Schunck, J. D. McDonnell, D. Higdon, J. Sarich, and S. Wild. Quantification of Uncertainties in Nuclear Density Functional Theory. *Nucl. Data Sheets*, 123:115, 2015.
- [17] Nicolas Schunck, Jordan D. McDonnell, Jason Sarich, Stefan M. Wild, and Dave Higdon. Error analysis in nuclear density functional theory. *J. Phys. G: Nucl. Part. Phys.*, 42(3):034024, 2015.
- [18] N. Schunck, J. D. McDonnell, D. Higdon, J. Sarich, and S. M. Wild. Uncertainty Quantification and Propagation in Nuclear Density Functional Theory. *Eur. Phys. J. A*, 51(12):1, 2015.
- [19] M. Beiner, H. Flocard, Nguyen Van Giai, and Ph. Quentin. Nuclear ground-state properties and self-consistent calculations with the skyrme interaction:(I). Spherical description. *Nucl. Phys. A*, 238(1):29, 1975.
- [20] E. Chabanat, P. Bonche, P. Haensel, J. Meyer, and R. Schaeffer. A Skyrme parametrization from subnuclear to neutron star densities. *Nucl. Phys. A*, 627(4):710, 1997.
- [21] E. Chabanat, P. Bonche, P. Haensel, J. Meyer, and R. Schaeffer. A Skyrme parametrization from subnuclear to neutron star densities Part II. Nuclei far from stabilities. *Nucl. Phys. A*, 635(1):231, 1998.
- [22] A. B. Brown. New Skyrme interaction for normal and exotic nuclei. *Phys. Rev. C*, 58(1):220, 1998.
- [23] S. G. Nilsson and I. Ragnarsson. *Shapes and Shells in Nuclear Structure*. Cambridge University Press, 1995.
- [24] T. Duguet. Symmetry broken and restored coupled-cluster theory: I. Rotational symmetry and angular momentum. *J. Phys. G: Nucl. Part. Phys.*, 42(2):025107, 2015.
- [25] T. Duguet and G. Hagen. Ab initio approach to effective single-particle energies in doubly closed

- shell nuclei. *Phys. Rev. C*, 85(3):034330, 2012.
- [26] Gianluca Colò, Hiroyuki Sagawa, and Pier Francesco Bortignon. Effect of particle-vibration coupling on single-particle states: A consistent study within the Skyrme framework. *Phys. Rev. C*, 82(6):064307, 2010.
 - [27] Li-Gang Cao, G. Colò, H. Sagawa, and P. F. Bortignon. Properties of single-particle states in a fully self-consistent particle-vibration coupling approach. *Phys. Rev. C*, 89(4):044314, 2014.
 - [28] D. Tarpanov, J. Dobaczewski, J. Toivanen, and B. G. Carlsson. Spectroscopic Properties of Nuclear Skyrme Energy Density Functionals. *Phys. Rev. Lett.*, 113(25):252501, 2014.
 - [29] J Dudek, B Szpak, M-G Porquet, and B Fornal. Statistical significance of theoretical predictions: A new dimension in nuclear structure theories (I). *J. Phys.: Conf. Ser.*, 267:012062, 2011.
 - [30] B Szpak, J Dudek, M-G Porquet, and B Fornal. Statistical significance of theoretical predictions: A new dimension in nuclear structure theories (II). *J. Phys.: Conf. Ser.*, 267:012063, 2011.
 - [31] J Dudek, B Szpak, B Fornal, and A Dromard. Predictive power and theoretical uncertainties of mathematical modelling for nuclear physics. *Phys. Scr.*, T154:014002, 2013.
 - [32] M. Bender, G. F. Bertsch, and P.-H. Heenen. Global study of quadrupole correlation effects. *Phys. Rev. C*, 73(3):034322, 2006.
 - [33] N. Nikolov, N. Schunck, W. Nazarewicz, M. Bender, and J. Pei. Surface symmetry energy of nuclear energy density functionals. *Phys. Rev. C*, 83(3):034305, 2011.
 - [34] N. Dubray and D. Regnier. Numerical search of discontinuities in self-consistent potential energy surfaces. *Comput. Phys. Commun.*, 183(10):2035, 2012.
 - [35] Y. M. Engel, D. M. Brink, K. Goeke, S. J. Krieger, and D. Vautherin. Time-dependent Hartree-Fock theory with Skyrme’s interaction. *Nucl. Phys. A*, 249(2):215, 1975.
 - [36] J. Dobaczewski and J. Dudek. Time-Odd Components in the Rotating Mean Field and Identical Bands. *Acta Phys. Pol. B*, 27(1):45, 1996.
 - [37] Michael Bender, Paul-Henri Heenen, and Paul-Gerhard Reinhard. Self-consistent mean-field models for nuclear structure. *Rev. Mod. Phys.*, 75(1):121, 2003.
 - [38] E. Perlińska, S. G. Rohoziński, J. Dobaczewski, and W. Nazarewicz. Local density approximation for proton-neutron pairing correlations: Formalism. *Phys. Rev. C*, 69(1):014316, 2004.
 - [39] T. Lesinski, M. Bender, K. Bennaceur, T. Duguet, and J. Meyer. Tensor part of the Skyrme energy density functional: Spherical nuclei. *Phys. Rev. C*, 76(1):014312, 2007.
 - [40] M. V. Stoitsov, J. Dobaczewski, W. Nazarewicz, S. Pittel, and D. J. Dean. Systematic study of deformed nuclei at the drip lines and beyond. *Phys. Rev. C*, 68(5):054312, 2003.
 - [41] M. V. Stoitsov, J. Dobaczewski, R. Kirchner, W. Nazarewicz, and J. Terasaki. Variation after particle-number projection for the Hartree-Fock-Bogoliubov method with the Skyrme energy density functional. *Phys. Rev. C*, 76(1):014308, 2007.
 - [42] Meng Wang, G. Audi, F. G. Kondev, W. J. Huang, S. Naimi, and Xing Xu. The AME2016 atomic mass evaluation (II). Tables, graphs and references. *Chinese Phys. C*, 41(3):030003, 2017.
 - [43] R. Navarro Perez, N. Schunck, R. D. Lasserri, C. Zhang, and J. Sarich. Axially deformed solution of the Skyrme–Hartree–Fock–Bogolyubov equations using the transformed harmonic oscillator basis (III) HFBTHO (v3.00): A new version of the program. *Comput. Phys. Commun.*, 220(Supplement C):363, 2017.
 - [44] M.V. Stoitsov, N. Schunck, M. Kortelainen, N. Michel, H. Nam, E. Olsen, J. Sarich, and S. Wild. Axially deformed solution of the Skyrme–Hartree–Fock–Bogoliubov equations using the transformed harmonic oscillator basis (II) HFBTHO v2.00d: A new version of the program. *Comput. Phys. Commun.*, 184(6):1592, 2013.
 - [45] Stefan M. Wild. Solving derivative-free nonlinear least squares problems with POUNDERS. In Tamas Terlaky, Miguel F. Anjos, and Shabbir Ahmed, editors, *Advances and Trends in Optimization with Engineering Applications*, pages 529–540. SIAM, 2017.
 - [46] R. J. Furnstahl, D. R. Phillips, and S. Wesolowski. A recipe for EFT uncertainty quantification in nuclear physics. *J. Phys. G: Nucl. Part. Phys.*, 42(3):034028, 2015.
 - [47] Dave Higdon, Jordan D. McDonnell, Nicolas Schunck, Jason Sarich, and Stefan M. Wild. A

- Bayesian approach for parameter estimation and prediction using a computationally intensive model. *J. Phys. G: Nucl. Part. Phys.*, 42(3):034009, 2015.
- [48] J. D. McDonnell, N. Schunck, D. Higdon, J. Sarich, S. M. Wild, and W. Nazarewicz. Uncertainty Quantification for Nuclear Density Functional Theory and Information Content of New Measurements. *Phys. Rev. Lett.*, 114(12):122501, 2015.
 - [49] A. W. Steiner. Moving beyond Chi-squared in nuclei and neutron stars. *J. Phys. G: Nucl. Part. Phys.*, 42(3):034004, 2015.
 - [50] R. Utama, J. Piekarewicz, and H. B. Prosper. Nuclear mass predictions for the crustal composition of neutron stars: A Bayesian neural network approach. *Phys. Rev. C*, 93(1):014311, 2016.
 - [51] R. Utama and J. Piekarewicz. Refining mass formulas for astrophysical applications: A Bayesian neural network approach. *Phys. Rev. C*, 96(4):044308, 2017.
 - [52] R. Utama and J. Piekarewicz. Validating neural-network refinements of nuclear mass models. *Phys. Rev. C*, 97(1):014306, 2018.
 - [53] Z. M. Niu and H. Z. Liang. Nuclear mass predictions based on Bayesian neural network approach with pairing and shell effects. *Phys. Lett. B*, 778:48, 2018.
 - [54] Léo Neufcourt, Yuchen Cao, Witold Nazarewicz, and Frederi Viens. Bayesian approach to model-based extrapolation of nuclear observables. *Phys. Rev. C*, 98(3):034318, 2018.
 - [55] Léo Neufcourt, Yuchen Cao, Witold Nazarewicz, Erik Olsen, and Frederi Viens. Neutron Drip Line in the Ca Region from Bayesian Model Averaging. *Phys. Rev. Lett.*, 122(6):062502, 2019.
 - [56] Z. M. Niu, H. Z. Liang, B. H. Sun, W. H. Long, and Y. F. Niu. Predictions of nuclear β -decay half-lives with machine learning and their impact on r -process nucleosynthesis. *Phys. Rev. C*, 99(6):064307, 2019.
 - [57] Christian P. Robert and George Casella. *Monte Carlo Statistical Methods (Springer Texts in Statistics)*. Springer-Verlag New York, Inc., Secaucus, NJ, USA, 2005.
 - [58] Carl Edward Rasmussen and Christopher K. I. Williams. *Gaussian Processes for Machine Learning*. Adaptive Computation and Machine Learning. MIT Press, Cambridge, Mass, 2006. OCLC: ocm61285753.
 - [59] Marc C. Kennedy and Anthony O’Hagan. Bayesian calibration of computer models. *J. R. Statist. Soc.*, 63(3):425, 2001.
 - [60] Marc C Kennedy and Anthony O’Hagan. Predicting the output from a complex computer code when fast approximations are available. *Biometrika*, 87(1):1–13, 2000.
 - [61] Dave Higdon, Marc Kennedy, James C Cavendish, John A Cafeo, and Robert D Ryne. Combining field data and computer simulations for calibration and prediction. *SIAM Journal on Scientific Computing*, 26(2):448–466, 2004.
 - [62] Dave Higdon, James Gattiker, Brian Williams, and Maria Rightley. Computer Model Calibration Using High-Dimensional Output. *J. Am. Statist. Assoc.*, 103(482):570, 2008.
 - [63] Rob Carnell. *lhs: Latin Hypercube Samples*, 2012. R package version 0.10.
 - [64] Fei Liu, MJ Bayarri, JO Berger, et al. Modularization in bayesian analysis, with emphasis on analysis of computer models. *Bayesian Analysis*, 4(1):119–150, 2009.
 - [65] F. Pedregosa, G. Varoquaux, A. Gramfort, V. Michel, B. Thirion, O. Grisel, M. Blondel, P. Prettenhofer, R. Weiss, V. Dubourg, J. Vanderplas, A. Passos, D. Cournapeau, M. Brucher, M. Perrot, and E. Duchesnay. Scikit-learn: Machine learning in Python. *Journal of Machine Learning Research*, 12:2825–2830, 2011.
 - [66] Bob Carpenter, Andrew Gelman, Matthew D Hoffman, Daniel Lee, Ben Goodrich, Michael Betancourt, Marcus Brubaker, Jiqiang Guo, Peter Li, and Allen Riddell. Stan: A probabilistic programming language. *Journal of Statistical Software*, 76(1), 2017.
 - [67] Andrew Gelman and Donald B Rubin. Inference from iterative simulation using multiple sequences. *Statistical Science*, pages 457–472, 1992.